The Thesis Committee for Aayush Agrawal
certifies that this is the approved version of the following thesis:

Sublimation and photodissociation in the LCROSS ejecta plume: Effects of lunar material

APPROVED BY

SUPERVISING COMMITTEE:

Matthew Hall, Supervisor

David B. Goldstein, Co-Supervisor

Philip L. Varghese

Sublimation and photodissociation in the LCROSS ejecta plume: Effects of lunar material

by

Aayush Agrawal

THESIS

Presented to the Faculty of the Graduate School of

The University of Texas at Austin

in Partial Fulfillment

of the Requirements

for the Degree of

MASTER OF SCIENCE IN ENGINEERING

THE UNIVERSITY OF TEXAS AT AUSTIN

May 2019

Sublimation and photodissociation in the LCROSS ejecta plume: Effects of lunar material

Aayush Agrawal, M.S.E.
The University of Texas at Austin, 2019

Supervisors: Matthew Hall
David B. Goldstein

The National Aeronautics and Space Administration (NASA) launched the Lunar Crater Observing and Sensing Satellite (LCROSS) mission to confirm the presence/absence of water ice and the nature of the regolith on the surface of the Moon. Previous workers [1, 2, 3] developed a numerical model to simulate the LCROSS impact and characterize the lunar regolith by comparing numerical results with the actual observations. In this study, we present an improved grain heating and sublimation model, and explore photodissociation of water ice as a potential source of observed hydroxyl in the impact plume. We consider icy grains with lunar regolith inclusions and calculate the absorption and emission efficiencies of the grains using Mie theory. The grains with regolith inclusions create a denser vapor cloud in the plume and thus a greater amount of hydroxyl. The hydroxyl obtained from *direct* photodissociation of ice in the grains is also an important component of hydroxyl observations made by LCROSS.

Table of Contents

Abstract **iv**

List of Tables **vi**

List of Figures **vii**

Chapter 1. Introduction **1**

Chapter 2. Literature Review **4**

Chapter 3. Grain Heating And Sublimation **10**
3.1 Mie Theory 14
3.2 Mie theory calculations for pure ice grains 18

Chapter 4. Regolith Materials **21**
4.1 Maxwell Garnett mixing rule 21
4.2 Optical properties of mixture of water ice and inclusions 23

Chapter 5. Grains With Inclusions **28**
5.1 Photodissociation of water vapor 38

Chapter 6. Direct Ice Photodissociation **41**
6.1 LCROSS OH count 52

Chapter 7. Conclusions **55**

Chapter 8. Recommendations for Future Work **57**

References **58**

List of Tables

5.1 Fraction of total ice particles that get sublimated at different times after the LCROSS impact (at t=0 s) for different values of f_{inc}. 33

5.2 Mass of OH ultimately produced from t=0 to 250 s from water vapor for different values of volume fractions of inclusions in the grain (f_{inc}). The inclusions are pyroxene and olivine. 39

6.1 Mass of OH produced from water vapor and directly from water ice for different values of volume fractions of inclusions of olivine in the grain (f_{inc}) 46

6.2 Mass of OH produced from water vapor and directly from water ice for different values of volume fractions of pyroxene inclusions in the grain (f_{inc}) and probability scaling parameter α 50

6.3 Mass of OH produced from water vapor and directly from water ice for different values of volume fractions of olivine inclusions in the grain (f_{inc}) and probability scaling parameter α 51

List of Figures

3.1 Different grain models implemented for the simulation of icy grains in the LCROSS impact plume. 11

3.2 Schematic diagram of the grain model used in the present study. 12

3.3 Curve of albedo of water ice grains vs radius for solar irradiation. 17

3.4 Contour plot of emitted heat flux as a function of grain radius and temperature. 18

3.5 Curves of grain radius vs time for several different initial grain sizes. 20

4.1 Curves of real and imaginary part of refractive index vs wavelength for olivine and pyroxene.. 24

4.2 Plot of intensity of solar radiation at 1 AU vs wavelength. λ=0.046-0.114 μm: blackbody radiation (5850 K); λ=0.114-2.412 μm: SORCE data ([4]); λ >2.412 μm: blackbody radiation (5850 K). 25

4.3 Curves of the real of the refractive index vs wavelength for composite material with pyroxene and olivine inclusions for several different values of f_{inc}. 25

4.4 Curves of the imaginary of the refractive index vs wavelength for composite material with pyroxene and olivine inclusions for several different values of f_{inc}. 26

5.1 Ice grain albedo vs grain radius for several different volume fractions of inclusions. 29

5.2 Curves of grain temperature vs time for several different initial grain size. The volume fraction of regolith inclusions in the grains is f_{inc}=0.2. 29

5.3 Curves of grain radius vs time for several grains that are 20% regolith by volume. 31

5.4 Grain lifetimes for a several values of volume fraction of inclusions. 32

5.5 Distribution of grain radii (count) at several instances of time during the LCROSS event for grains containing pyroxene and olivine. 36

5.6 Column Density of water vapor for pure water ice. 37

5.7 Column density of water vapor for dirty water ice. The cloud of water vapor formed due to sublimation is larger and denser due to the presence of regolith inclusions in the grains, much more so for olivine inclusions than pyroxene inclusions. 37

6.1 Average value of absorptance as a function of grain radius for solar radiation in $45 - 242\ nm$ for several different volume fractions of inclusions in the grain. 44

6.2 Total number of OH molecules in the FOV from photodissociation of vapor/ice molecules in the grains. The curves are for several different values of volume fraction of pyroxene and olivine inclusions. 54

Chapter 1

Introduction

The National Aeronautics and Space Administration (NASA) launched the Lunar Crater Observing and Sensing Satellite (LCROSS) mission along with the Lunar Reconnaissance Orbiter (LRO) on June 18, 2009. The LCROSS mission was launched in order to confirm the presence/absence of water ice and the nature of the regolith in the permanently shadowed regions (PSR) of the Moon. The Atlas V Centaur upper-stage rocket (Centaur rocket) was directed by the Shepherding Spacecraft (S-SC) to impact the Cabeus crater near the south pole of the Moon. The S-SC followed the Centaur rocket with a delay of four minutes to observe the plume created by the impact. Heldmann et al. [5], Schultz et al. [6], Colaprete et al. [7], Colaprete et al. [8], Heldmann et al. [9] and others have reported the initial observations and findings of the mission.

Goldstein et al. [1], Summy et al. [2], Heldmann et al. [3] published a series of research articles which presented the simulation of the LCROSS impact plume. The successive articles detail the improvements made in the LCROSS numerical model including the sublimation of water molecules from sun warmed regolith grains in the illuminated plume. The numerical approach

was improved by constraining the model and examining various possible plume parameters based on spacecraft observations. The authors analyzed data from the UV-visible spectrometer (VSP), specifically the VSP light curve, hydroxyl emission data and the color evolution of VSP spectra, and compared the data with the numerical results [3].

The study presented here represents further improvements to the numerical grain model. We present an improved grain heating model with optical properties of the grains calculated using the Mie Theory for electromagnetic radiation. Grains with regolith inclusions are considered and the presence and effect of different regolith materials on the heating and sublimation of the grains is studied. Direct photodissociation of water ice from the grains is also examined as an additional mechanism for production of hydroxyl observed in the plume by S-SC.

The study present in this thesis is adapted from a research article [10] titled "Characterizing the hydroxyl observation of the LCROSS UV-Visible spectrometer: Modeling of the impact plume" by Poondla, Y. et. al., yet to be published. Some segments of the thesis have been taken verbatim from the article. The LCROSS grain model presented in Chapter 3 is an improvement first made by Yasvanth Poondla (YP), a member of the Computational Flow Physics Laboratory (CFPL) in the Department of Aerospace Engineering and Engineering Mechanics at the University of Texas, Austin. The improvement in the grain heating model is described in this study for the sake of completeness. The initial analysis with the lunar material pyroxene as inclusions in the

grains was also carried out by Yasvanth Poondla. I have performed a similar analysis with another lunar material, olivine, and compared the properties of grains containing pyroxene and olivine inclusions.

The thesis is organized as follows. In Chapter 2, the work done on the topic is discussed. In Chapter 3, the improved grain heating model by YP along with brief description of the Mie theory is presented. Chapter 4 presents the differences in the optical properties of grains containing pyroxene and olivine inclusions, and Chapter 5 presents a detailed Mie theory analysis of the grains with inclusions. Chapter 6 discusses in detail the role of direct photodissociation of water ice in the LCROSS ejecta plume. Chapter 7 presents the major conclusions that can be drawn from the study and Chapter 8 discusses further improvements that can be made to improve the fidelity of the present study.

Chapter 2

Literature Review

The LCROSS mission utilized two spacecraft, the Atlas V Centaur upper-stage (Centaur rocket) and the Shepherding Spacecraft (S-SC). The Centaur rocket impacted the Cabeus crater near the south pole of the Moon at 84.675^oS, -48.703^oE. The two lunar impacts, Centaur rocket impact and S-SC impact, occurred on October 9, 2009 at 11 : 31 : 19.506 UTC and 11 : 35 : 36.116 UTC respectively. The Centaur rocket which acted as a kinetic impactor (2366 kg mass) was directed by the S-SC to create a controlled impact plume similar to comet impacts. S-SC followed the Centaur rocket's trajectory with a delay of four minutes and observed the properties of the impact plume before impacting the Moon itself. The plume created by the impact was observed by nine scientific instruments aboard S-SC. The Cabeus crater floor has a depth of 833 m below the shadow cast by the rim, and the impact plume was only expected to be observable above this altitude. The site was selected keeping in mind the appropriate solar illumination of the impact plume, in order to observe it with S-SC instrumentation, LRO and Earth-based telescopes.

The LCROSS payload included nine scientific instruments: a visible

camera (VIS) developed by Ecliptic Enterprises Corporation; two near infrared cameras (NIR) (0.9-1.7 μm) from Goodrich Sensors Unlimited; two mid infrared cameras (MIR) ($6.0 - 13.5$ μm), one from Thermoteknix Ltd. and other from Flir Systems/Indigo Operations; a Total Luminance Photometer (TLP) designed by NASA Ames Research Center; an ultraviolet-visible spectrometer (VSP) from Ocean Optics, Ltd.; two near infrared spectrometers (NSP) manufactured by Polychromix. Along with these instruments, the payload also consisted of a central data handling unit (DHU). The DHU was also provided by Ecliptic Enterprises and collected data from the instruments and relayed it back to NASA. The details of these instruments can be found in Ennico et al. [11].

Direct human and robotic exploration is inhibited in the PSR due to extremely low temperatures. Thus, the LCROSS mission is significant as it provided the first *in situ* exploration of the PSR. Also, meteoroid impacts have been observed by NASA (Suggs et al. [12]), but the controlled and pre-planned impact in the LCROSS mission enabled the advance planning of observations to be taken with spacecraft instrumentation and Earth based instruments. Since water is such a crucial resource, identifying its presence and the nature of its disposition on the Moon could assist in efforts to establish a long term human presence elsewhere in the solar system. Characterization of the regolith can also help answer more fundamental questions regarding the formation and evolution of planetary atmospheres.

Several ways have been proposed theoretically for the water to reach

the lunar surface. Water can be generated by solar wind, deposited by H_2O-containing meteoroids and comets, and degassed from the interior (Arnold [13], Needham and Kring [14]). Studies (Butler [15], Crider and Vondrak [16], Stewart et al. [17], Prem et al. [18] etc.) suggest that some of this water can migrate to the polar cold traps from deposits elsewhere. In general, water vapor on the Moon is rapidly lost by Jeans escape and photo-chemical or solar wind knock-on collisions. However, some permanently shadowed regions have surface temperatures as low as 25 K (Vasavada et al. [19], Paige et al. [20]), which allows water and other volatiles to become trapped. These trapped volatiles can remain stable for billions of years. One of the aims of the LCROSS mission was to determine the composition of volatiles within the lunar regolith in the PSR.

Before the mission, numerical and analytical models made predictions of observable results and provided information required for planning the mission and observations. Heldmann et al. [21] presented a compilation of model results which provided some estimates for the impact event. Goldstein et al. [1] examined the dust, water and vapor dynamics due to the impact using a free molecular model. Photo-dissociation and ionization of water molecules were included in the model. Shuvalov and Trubetskaya [22] simulated the LCROSS impact using a crater formation model with the SOVA hydrocode (Shuvalov [23]). Korycansky et al. [24] modeled the LCROSS impact using a large scale smooth particle hydrodynamics (SPH) code, finite difference hydrodynamics codes, and semi-analytic calculations using a Monte Carlo method and scal-

ing models. Davis [25] studied the evolution of the impact plume through a theoretical model based on gas dynamics and thermodynamics. These studies along with others assisted in preparing for the experiment.

After the mission, numerical models were utilized for understanding the evolution of the impact plume. These models may be validated from the observations obtained from the mission and can then be used further for obtaining a physical understanding of the evolution of the plume. Hurley [26] and Hurley et al. [27] used a Monte Carlo model to simulate the LCROSS impact: while Hurley [26] carried out a parametric study to evaluate the response of change in parameters characterizing the physical conditions on the evolution of the impact plume, Hurley et al. [27] presents a detailed analysis of the results and comparison with observed data.

Building on the work of Goldstein et al. [1], Summy et al. [2] simulated the LCROSS impact including the sublimation of water molecules from sun warmed regolith grains in the illuminated plume. Heldmann et al. [3] improved the numerical model by constraining the model and examining various possible plume parameters based on spacecraft observations. The authors [3] analyzed data from the VSP, specifically the VSP light curve, hydroxyl emission data and the color evolution of VSP spectra, and compared the data with the numerical results.

Many researchers have used Mie theory to study the scattering of dust particles in outer space systems. Artymowicz [28] studied the particle dynamics and size distribution of the particles in the β-Pictoris system by calculating

the extinction, scattering, and absorption efficiency factors and the radiation pressure coefficient for a spherical grain through Mie theory. Debes et al. [29] used Mie scattering models to determine scattering efficiency (Q_{sca}) of the HR 4796A disk for a given dust distribution. Kobayashi et al. [30, 31] studied the dependence of dust ring formation on materials and structures of dust particles using Mie theory to calculate the absorption efficiency for their sublimation model. Inoue et al. [32] conducted a similar study to obtain the spatial distribution of ice on the surface of the circumstellar disk around young stars. Beer et al. [33] developed a grain evolution model to simulate the behavior of icy grains in a comet c oma. They computed the efficiency and re-radiation of sunlight for grains using the Mie theory. We do similar calculations in the present work to calculate the optical properties of the grains.

Direct photodissociation of ice has also been extensively studied to interpret data for icy satellites of the giant planets. Johnson and Quickenden [34] discuss the radiolysis and photolysis of water ice in the outer solar system and summarize the available experimental data. Delitsky and Lane [35, 36] studied the radiolysis of pure H_2O and CO_2 ice and suggest species that might be observed as a result. The study was conducted for the icy satellites of Jupiter. Gerakines et al. [37] performed ultraviolet photolysis of a H_2O:CO_2 mixture using 10 eV photons to study the formation of carbonic acid (H_2CO_3). Quickenden et al. [38] studied the effect of temperature on electron irradiated water ice and determined the radiolytic yield of OH. Grigorieva et al. [39] developed a photosputtering model to estimate the erosion of icy silicate grains

in the β-Pictoris system. They investigated the effect of sublimation and photosputtering as a function of grain size, composition, and distance from the star. A similar study is conducted here to investigate the photo-desorption (sublimation and photodissociation) of icy grains on the surface of the Moon.

The motivation for this work is to better explain S-SC observed OH band strength. We improve the model associated with grain heating and sublimation, and introduce direct photodissociation as another source of observed OH. The results obtained through this study are post processed and fitted to the actual LCROSS observations to better characterize the impact plume and the physical conditions of the lunar regolith. This process is done by Sergio Tovar (ST), a co-member of the Computational Flow Physics Laboratory (CFPL) in the Department of Aerospace Engineering and Engineering Mechanics at the University of Texas, Austin.

Chapter 3

Grain Heating And Sublimation

Note: This chapter presents the improvements in the grain heating model made by YP along with a brief description of Mie theory for electromagnetic radiation. Mie analysis of pure ice grains is also presented which was also carried out by YP. The majority of this chapter is taken from our joint publication [10], and is presented here for the sake of continuity. The parts discussing grain heating model and Mie theory calculations in this chapter were written by YP for inclusion as a section in our publication.

The initial grain model used in earlier LCROSS simulations was discussed in detail in Heldmann et al. [3]. In LCROSS impact plume simulations, ice and dust grains are simulated using a free molecular approach. The grains are generated from a disk of lofted material centered around the location of impact of the LCROSS satellite. The grains are created from the disk assuming a random, uniform distribution from the center of the disk. In Heldmann et al. [3], two grain models are implemented (see Fig. 3.1): a single species icy shell model and a two species model. In the icy shell model, the grains are modeled as refractory regolith core with a thin shell of volatile ice around the core making up 6% ice by mass (model 1 in Fig. 3.1). In the two species

model, the grains are either pure ice or pure refractory regolith (model 2 in Fig. 3.1). Again the ice grains make up 6% of the total plume mass. Through the LCROSS observations, Colaprete et al. [7] estimated the concentration of water ice in the regolith at the LCROSS impact site to be 5.6±2.9% by mass. Hence, in all our models, grains contain 6% water ice by mass.

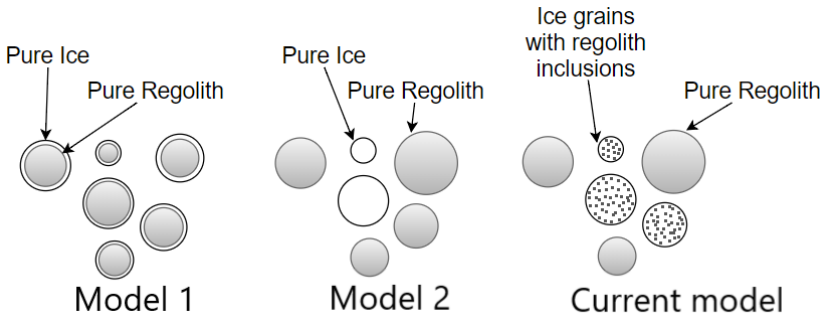

Figure 3.1: Different grain models implemented for the simulation of icy grains in the LCROSS impact plume.

Figure 3.2 shows the schematic diagram of the grain model used in the present study. The grains are created with a lognormal size distribution with an average radius $\mathcal{O}(1\ \mu\text{m})$, and velocity is determined based on the grain's distance from the center of the disk ([40]). Each grain consists of fixed number of particles which is same for all the grains. Thus larger (smaller) grains contain particles having large (small) size. All particles of a particular grain have the same size. Each particle of the grain is a simulation molecule which represent a large number of real molecules (water ice and regolith). Only the grains which have sufficient vertical velocity to leave the 833 m deep shadow region of the crater are considered. As the icy grains enter sunlight,

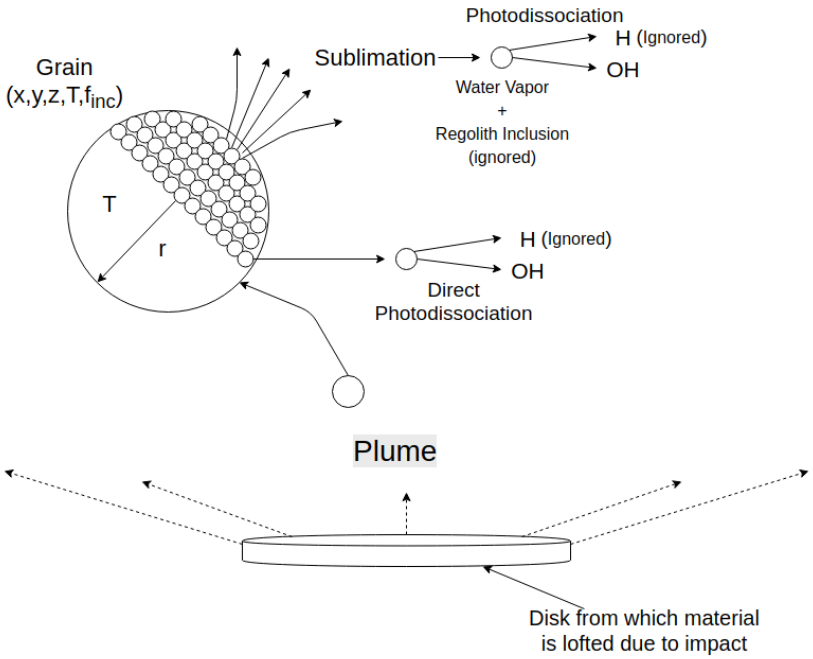

Figure 3.2: Schematic diagram of the grain model used in the present study.

they begin to warm up and sublime, releasing water vapor particles. The sublimated water vapor particles can then photodissociate, producing OH. The ice particles which do not sublimate, can photodissociate directly to produce OH which is discussed in Chapter 6. We ignore the regolith particles and hydrogen particles produced after photodissociation in the present study. The real number of molecules present as vapor/ice/hydroxyl are calculated from the particles present in these forms. Thus, the LCROSS simulation model used for this study is a Monte Carlo (MC) model where we study the evolution of LCROSS impact plume using probabilistic simulation. Note that in the current grain model, not all grains contain water ice. Only some of the grains contain

water ice such that the net mass of water ice is 6% of the total mass present in the impact plume. The fraction of total grains containing water ice depends on f_{inc}. 6% water ice by mass corresponds to f_{inc}=0.814 i.e. if f_{inc}=0.814, each grain would contain 6% water ice by mass and all of the grains in the simulation would contain both water ice and regolith.

Initially, the only parameter that varied in the heating model [3] was the grain albedo. The simulation of Heldmann et al. [3] used an albedo of 0.9 or 0.1, corresponding to the pure ice/pure dirt or icy shell grain model, respectively. The value of 0.9 was based on albedo data for bulk snow [41], which is an aggregate of ice grains with some size distribution. This aggregate value, however, is not the value for an individual grain, and its use introduces inaccuracies in the grain heating model. Furthermore, optical properties may vary with grain size. Based in part on work done by Beer et al. [42], Mie scattering theory calculations are therefore used to determine albedo and other optical properties of interest for individual water ice grains, and to determine how those properties vary with grain size. This is discussed in detail in Chapter 5.

The basic form of the grain heating model is described in Heldmann et al. [3]. The heating model operates on each individual grain and balances energy absorbed due to sunlight, energy lost due to radiation, and energy lost due to sublimation. The heating model can be expressed mathematically as:

$$\frac{dT}{dt} = \frac{A(\frac{1-\alpha(r)}{4}\phi_{total} - E_{emis}(r,T)) - \dot{m}_{sub}(c_{pi}T + \Delta H_{sub})}{m_i c_{pi} + m_d c_{pd}}, \qquad (3.1)$$

where T is the temperature of the grain, t is time, A is the surface area of the spherical grain, $\alpha(r)$ is the size dependent albedo of the grain, $E_{emis}(r,T)$ is the energy emitted by the grain at T, $\dot{m}_{sub}$ is the rate of sublimation, c_{pi} is the specific heat of ice, c_{pd} is the specific heat of the regolith, ΔH_{sub} is the enthalpy of sublimation and m_d is the mass of regolith in the grain.

In the present work, the optical properties of grains are calculated using Mie theory. The energy absorbed term ($\phi_{total}\left(\frac{1-\alpha}{4}\right)$) now uses the updated radius dependent albedo instead of a constant. The energy radiated term ($\varepsilon\sigma T^4$) is replaced entirely by a value interpolated from a lookup grid based upon Fig. 3.4 tabulating power emitted for a suitable range of grain radii and temperatures. The model uses a fourth order Runge-Kutta time integration method. For stability, a substepping model is also implemented, with the grain temperature used as a parameter to determine the exact number of substeps. In the present model, we assume the material lofted in the plume is in the form of spherical grains which is an approximation. However, the grains lofted due to the impact can acquire any odd shape which would have different optical properties from the spherical grains. But with random orientations, these odd shapes should, in bulk, appear spherical

3.1 Mie Theory

Here we discuss, in brief, the Mie theory for electromagnetic radiation. Wiscombe [43] provides a detailed description of Mie scattering theory. Mie theory is a solution to Maxwell's equations for a homogeneous dielectric sphere

subjected to an electromagnetic plane wave. The infinite series solution describes the scattering of the electromagnetic wave by such a sphere. Mie theory uses the refractive index of the dispersing medium to predict the intensity of the scattered light. Using the Mie solution, the absorbed, transmitted, and reflected electromagnetic radiation can be calculated for different particle sizes and complex index of refraction.

For the present work, the computational solver developed by Wiscombe [43] is used. The solver takes size parameter (x) and complex refractive index ($\underline{n}$) as inputs :

$$x = \frac{2\pi r}{\lambda}, \tag{3.2}$$

$$\underline{n} = n + ik, \tag{3.3}$$

where r and λ are the grain radius and wavelength of incident light, respectively. The imaginary component of the complex refractive index, k, is also known as the extinction coefficient. For water ice, the complex refractive index as a function of wavelength has been well documented (Wiscombe and Warren [41]).

The solver (Wiscombe [43]) outputs scattering and extinction efficiencies (Q) as a function of wavelength (for a given sphere). These efficiencies are the scattering cross sections normalized by the grain's projected area (πr^2).

Absorption efficiency is of particular interest for the current study (Eq. (3.1)), and can be calculated from scattering and extinction efficiency:

$$Q_{abs} = Q_{ext} - Q_{scat} \tag{3.4}$$

Albedo (α), defined here as the fraction of incident energy not absorbed by a grain, can be calculated by integrating the product of absorption efficiency and solar irradiance, and normalizing by total irradiance.

$$1 - \alpha = \frac{1}{\Phi_{total}} \int_0^\infty Q_{abs}(\lambda)\Phi_{sun}(\lambda)\mathrm{d}\lambda \tag{3.5}$$

$$\Phi_{total} = \int_0^\infty \Phi_{sun}(\lambda)\mathrm{d}\lambda \tag{3.6}$$

The integral in Eqs. (3.5) and (3.6) is calculated numerically with a discrete sum, and truncated at 10 μm, which accounts for 99.998% of the total solar irradiance. The solar irradiance data used for this work is a combination of the Solar Radiation and Climate Experiment (SORCE) satellite data on the day of the LCROSS mission and blackbody irradiance at 5850 K for wavelengths outside of the SORCE measurement region ([4]). SORCE satellite data is available for wavelengths 114-2412 nm. Repeating this calculation for different grain sizes yields the curve shown in Fig. 3.3.

The most important result is that albedo for micron-scale ice grains is larger than the aggregate-based value of 0.9. The small lofted ice grains with albedo values very close to 1 scatter nearly all of the incident sunlight. Even

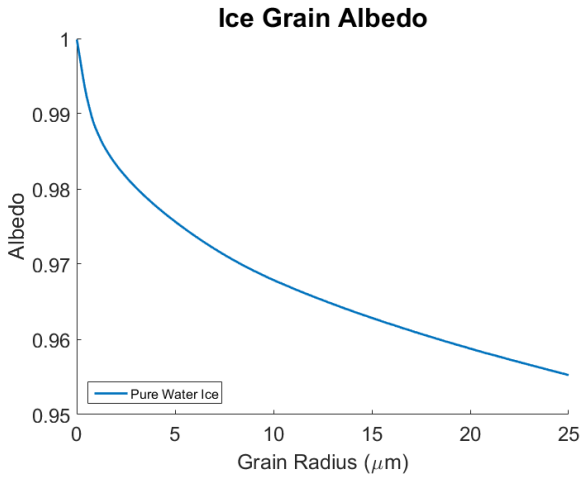

Figure 3.3: Curve of albedo of water ice grains vs radius for solar irradiation.

for larger grains, the albedo is greater than 0.9 which indicates that pure ice grains absorb very little energy from sunlight and thus should have very long sublimation lifetimes. As mentioned previously, the grain heating model has absorption, emission, and sublimation in the energy balance. Similar to the albedo calculation, calculation for emission of energy is also carried out using Mie theory. The product of emission efficiency and Planck's law is integrated over a suitable wavelength range, for a range of grain sizes and temperatures.

$$E_{emis} = \int_0^\infty Q_{abs}(\lambda)\Phi_{Planck}(\lambda)\mathrm{d}\lambda \tag{3.7}$$

Figure 3.4 shows the emitted power from a grain as a function of grain temperature and size. Clearly, warmer grains yield a larger thermal flux. Power emitted increases with grain size for small grains, at warm (∼120-160K) temperatures. Energy emitted varies with temperature as T^4, but is relatively

constant with respect to radius. The exception is at small grain radii, where a steep drop off in energy emitted is present. Using the data obtained from Mie theory calculations for emission and absorption of energy from a grain, we can analyze the evolution of the grain radius and temperature in sunlight.

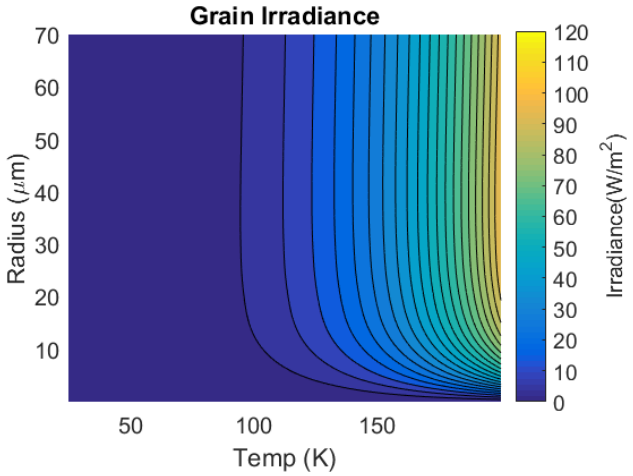

Figure 3.4: Contour plot of emitted heat flux as a function of grain radius and temperature.

3.2 Mie theory calculations for pure ice grains

We now use a standalone grain heating model (Eq. (3.1)) to obtain insight into how grains warm up and sublimate. Optical properties of pure ice grains calculated using Mie Theory are used (Figs. 3.3 and 3.4). The lifetime of the grains can be broken up into three portions: a slow, roughly linear sublimation portion, a rapid, nonlinear portion, and a final portion characterized by negligible sublimation. The first two portions of the lifetime can be seen in Fig. 3.5(a) for larger grains. The final lifetime portion can

be seen in Fig. 3.5(b) for sub-micron grains. The majority of the lifetime for the larger grains (>10 μm) is made up of the initial linear portion. Smaller grains do not even experience this linear portion during their lifetimes. Note that although we call the second lifetime portion rapid, it is still a long period of time; the grain of size 7 μm (cf. Fig. 3.5(a)) has a lifetime of 50 million seconds or 1.5 years. Fig. 3.5(b) shows curves of lifetime for submicron sized grains to demonstrate the final portion of the grain lifetime. As the grain radius approaches 0.01 μm, the sublimation rate decreases rapidly and the grain radius becomes nearly constant. Most of the grain mass for these small grains sublimes in the first 10-20% of its lifetime. In the code, we stop the simulation when the radius of the grain reaches 0.01 μm to avoid running the code for a very long period of time. This is because, at this size the sublimation rate drops off rapidly and the grain becomes nearly constant in size. The time at which the radius of the grain becomes equal to 0.01 μm is defined as the lifetime of the grain in the present study.

From these calculations, it is apparent that pure water ice grains with size larger than a micron last much longer than the LCROSS observation timescale of 250 s. Based on the analysis done above, the sublimated water vapor coming from pure ice grains would be a very small fraction of the total mass of lofted water. This does not agree with conclusions drawn from an analysis of the observations (Colaprete et al. [44]). One possible explanation for this is that the lofted water ice is not pure and instead contains inclusions of dark lunar regolith (discussed in Chapter 5).

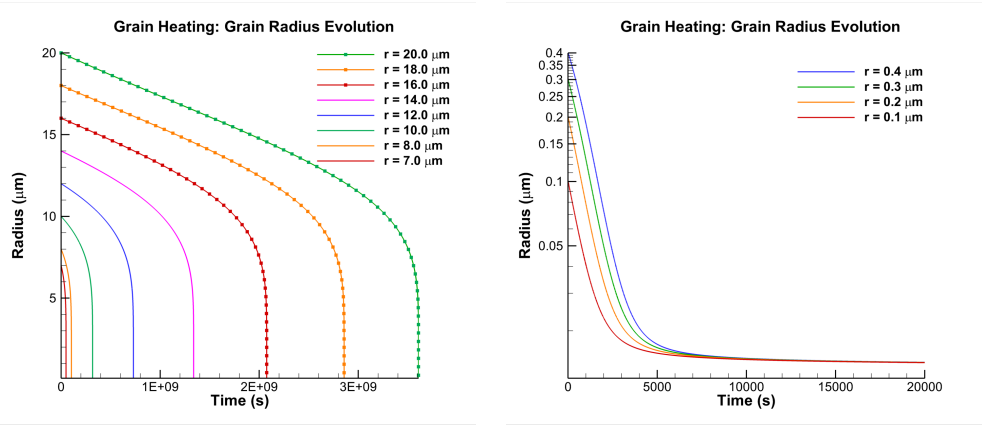

(a) Micron sized grains

(b) Submicron sized grains

Figure 3.5: Curves of grain radius vs time for several different initial grain sizes.

Chapter 4

Regolith Materials

Note: Use of the Maxwell-Garnett mixing rule to calculate effective dielectric function of the homogeneous mixture was first done by YP with regard to the study presented here. The description of the Maxwell-Garnett mixing rule in Section 4.1 is taken from a section (written by YP) of our joint publication [10].

Here we examine the possibility that a source of the observed water vapor/OH was from grains of ice darkened by regolith inclusions that thereby warm and sublimate faster than pure ice grains. Therefore we need to calculate the optical properties of grains comprising a mixture of ice and regolith. To do this, we need to find the effective imaginary refractive index of the mixture of ice and regolith. Of the numerous effective medium approaches that exist, we use the Maxwell-Garnet mixing rule to model icy grains with regolith inclusions (Mukai [45]).

4.1 Maxwell Garnett mixing rule

The Maxwell Garnett mixing rule calculates an effective dielectric function, ϵ, given the dielectric functions for a medium and inclusion(s), and the

volume fraction of those inclusion(s). The dielectric function (complex) is a measure of a material's permittivity to an electric field. The M-G mixing rule is given as:

$$\epsilon_{av} = \epsilon_{med}[1 + \frac{3f_{inc}(\epsilon_{inc} - \epsilon_{med})(\epsilon_{inc} + 2\epsilon_{med})^{-1}}{1 - f_{inc}(\epsilon_{inc} - \epsilon_{med})(\epsilon_{inc} + 2\epsilon_{med})^{-1}}], \tag{4.1}$$

where ϵ_{av} is the effective dielectric function, ϵ_{inc} and ϵ_{med} are the dielectric functions of the inclusions and medium respectively, and f_{inc} is the total volume fraction of the inclusions. Here we have simplified our analysis to consider inclusions of only a single material, either olivine or pyroxene. A more appropriate assumption would be to have inclusions of multiple regolith materials which would introduce more unknown parameters. As discussed in Section 3.1, the selected Mie code requires as input a complex refractive index, which is related to the complex dielectric function by the following relations Hecht [46]:

$$\epsilon = \epsilon_r + i\epsilon_i, \tag{4.2}$$

$$\epsilon_i = -2nk, \tag{4.3}$$

$$\epsilon_r = n^2 - k^2, \tag{4.4}$$

where ϵ_r and ϵ_i are the real and imaginary part of the dielectric function respectively.

4.2 Optical properties of mixture of water ice and inclusions

Pyroxene and olivine, which are both types of silicate minerals were chosen as suitable representatives of lunar regolith, since they are estimated to be major constituents of lunar regolith (Heiken et al. [47]). The refractive indices of pyroxene and olivine are gathered from Jäger et al. [48] and Draine and Lee [49], respectively.

For the new grain model, we choose a total volume fraction of inclusions, either pyroxene or olivine, and assume that the inclusions are such that the spherical particle is homogeneous. It is assumed that the medium is water ice, and the inclusions are silicate. In order to further simplify the analysis, we also assume that the composition of the grain with inclusions do not change as it sublimates. Physically, this model implies that some inclusions leave the grain such that the volume fraction remains constant as it sublimates.

Figure 4.1 shows the curves of the real part and imaginary part of the refractive index for the lunar regolith materials olivine and pyroxene for the wavelength up to 5 μm. The real part of the refractive index characterizes the scattering of electromagnetic radiation while the imaginary part of the refractive index characterizes the absorption of electromagnetic radiation. It can be seen that the real part is almost identical for both the lunar materials but there is a considerable difference in the imaginary part of the refractive index between the two materials. The values of k for olivine are much higher than those of pyroxene (more than an order of magnitude higher).

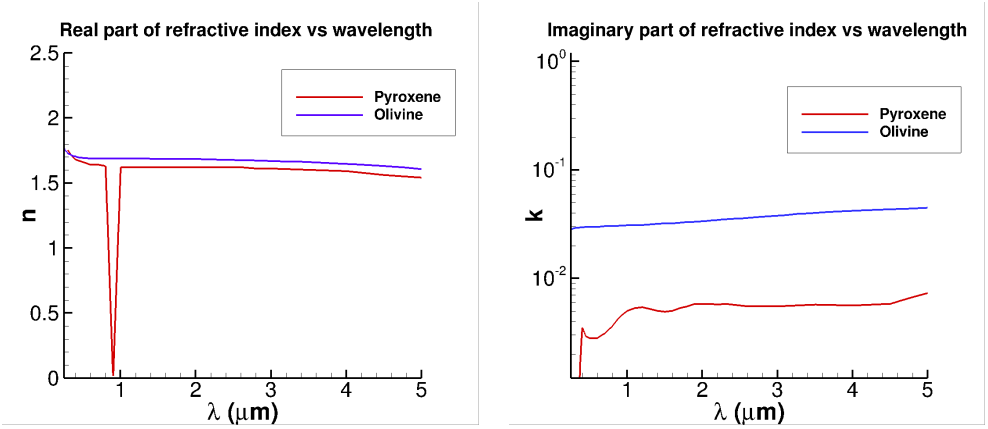

(a) Real part of refractive index (b) Imaginary part of refractive index

Figure 4.1: Curves of real and imaginary part of refractive index vs wavelength for olivine and pyroxene..

Figure 4.2 shows the intensity of solar radiation at 1 AU for the wavelengths up to 10 μm. As discussed in Section 3.1, the combination of SORCE satellite data and blackbody radiation at 5850 K are used for this study. The major fraction of the total solar energy is contained in the wavelength range 0.2-4 μm.

As per Mie theory, the energy absorbed by a spherical grain depends on the size parameter and the imaginary part of refractive index. As either increases, the absorbed energy increases. In case of olivine, the imaginary part of the refractive index is much higher than that of pyroxene and thus olivine should absorb much more energy than pyroxene. This is confirmed in Chapter 5 through the detailed Mie theory calculations. As the real part of refractive index for the two materials does not differ significantly, we can expect similar scattering of solar radiation from the two materials.

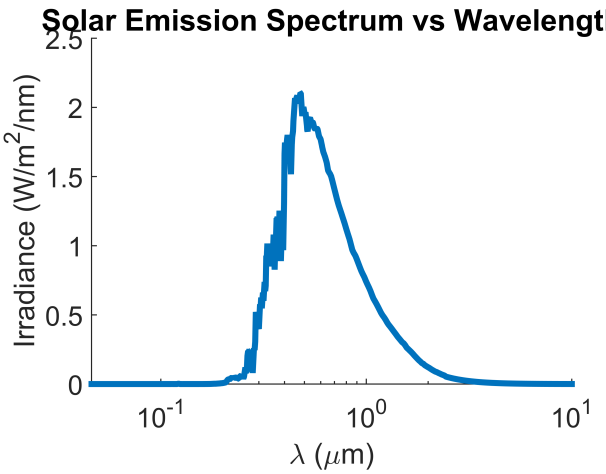

Figure 4.2: Plot of intensity of solar radiation at 1 AU vs wavelength. λ=0.046-0.114 μm: blackbody radiation (5850 K); λ=0.114-2.412 μm: SORCE data ([4]); λ >2.412 μm: blackbody radiation (5850 K).

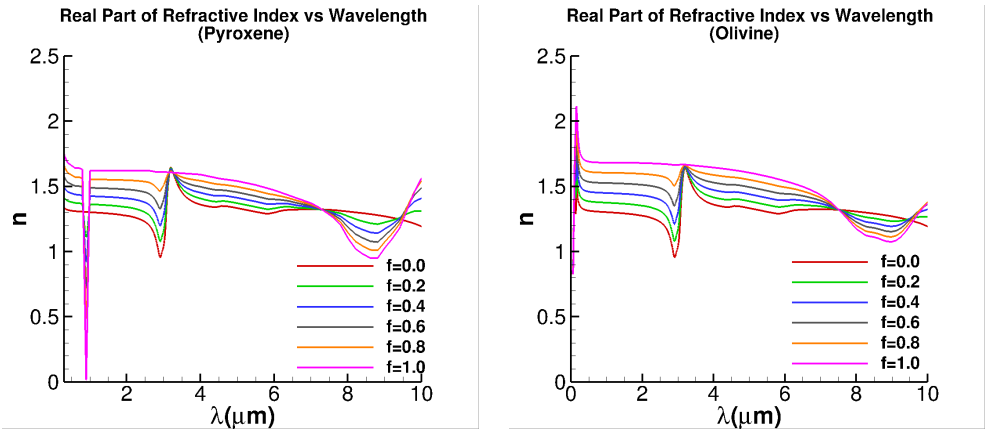

(a) Pyroxene inclusions

(b) Olivine inclusions

Figure 4.3: Curves of the real of the refractive index vs wavelength for composite material with pyroxene and olivine inclusions for several different values of f_{inc}.

Figures 4.3 and 4.4 show the real and imaginary part of the refractive index for water ice having inclusions of pyroxene and olivine for several

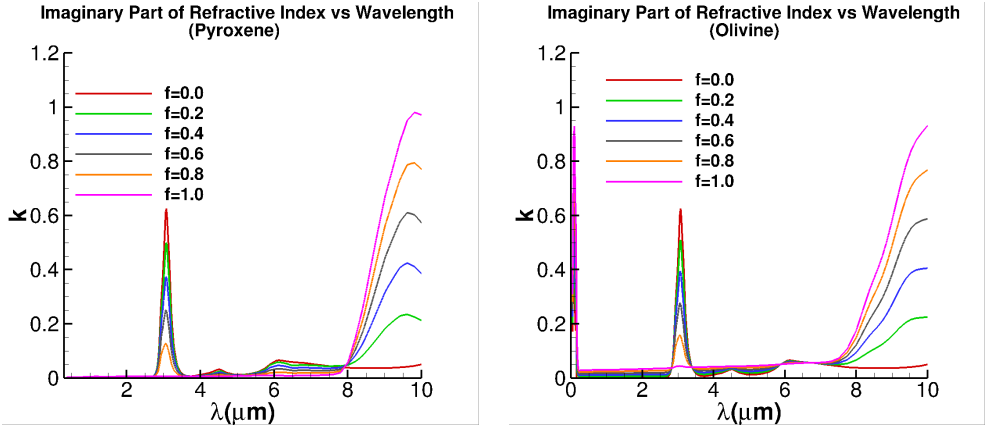

(a) Pyroxene inclusions (b) Olivine inclusions

Figure 4.4: Curves of the imaginary of the refractive index vs wavelength for composite material with pyroxene and olivine inclusions for several different values of f_{inc}.

different values of f_{inc}. The properties presented in Figs. 4.3 and 4.4 were calculated using the M-G mixing rule (Eq. (4.1)). The inclusion of regolith material does generally increase the refractive index which would lead to a decrease in albedo compared to pure ice grains. Again, the imaginary part of the refractive index of grains with olivine is much higher than that of pyroxene in the wavelength range 0.2-3 μm (see Fig. 4.4) where most of the solar energy is concentrated. Therefore the grains with olivine should absorb more energy compared to grains with pyroxene. As for the scattering of solar radiation, we expect grains with both type of inclusions to behave in a similar manner. Around 3 μm, the value of the imaginary part of the refractive index for pure ice has a sharp increase. In the small wavelength band near 3 μm, we would expect the grains with larger fraction of ice to absorb more energy. However as

the intensity of energy for this wavelength band is very low (see Fig. 4.2), no significant effect on the overall optical properties of the grains should be expected. The optical properties of grains with inclusions is discussed in further detail in Chapter 5.

Chapter 5

Grains With Inclusions

Note: The detailed Mie theory analysis for pyroxene presented in this chapter was first done and written by YP for our joint publication [10]. However, the detailed analysis for olivine and subsequent comparison between grains having pyroxene and olivine inclusions is done by me. Some of the sentences present in this chapter have been written by YP and are taken verbatim.

In this section, we present the optical properties of ice grains with pyroxene and olivine inclusions. The effect of these inclusions on the sublimation of the grains is also presented. We perform the Mie analysis as before (ref. Section 3.1) using the refractive index for the mixture of ice and regolith shown in Chapter 4. We find that the albedo and therefore the lifetimes of the grains decrease with an increasing volume fraction of regolith (see Figs. 5.1 and 5.4). For high values of f_{inc}, the albedo of the grains having olivine inclusions decreases rapidly for grain sizes above 0.1 μm, while for grains having pyroxene inclusions, the albedo starts decreasing for grain sizes above 1 μm. However the albedo values still converge to a value of 1 for very small grain sizes ($<$ 0.1 μm). This difference can be attributed to an order of magnitude difference

between the values of imaginary part of the refractive index of olivine and pyroxene for wavelengths 0.2-4 μm.

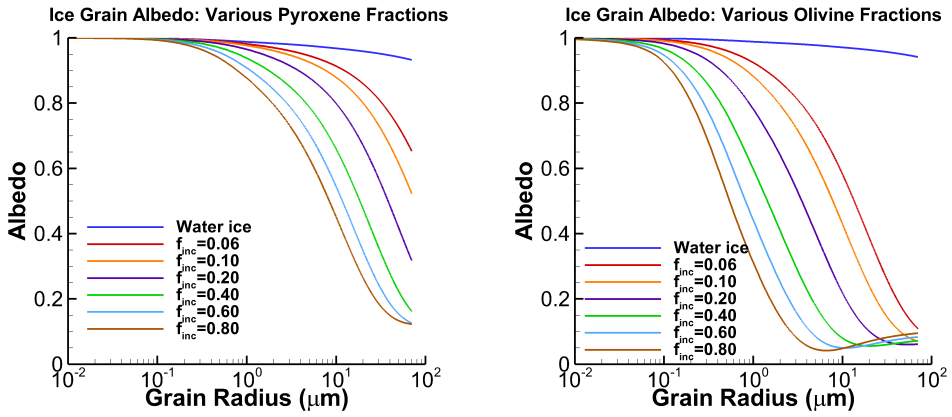

(a) Grains with pyroxene (b) Grains with olivine

Figure 5.1: Ice grain albedo vs grain radius for several different volume fractions of inclusions.

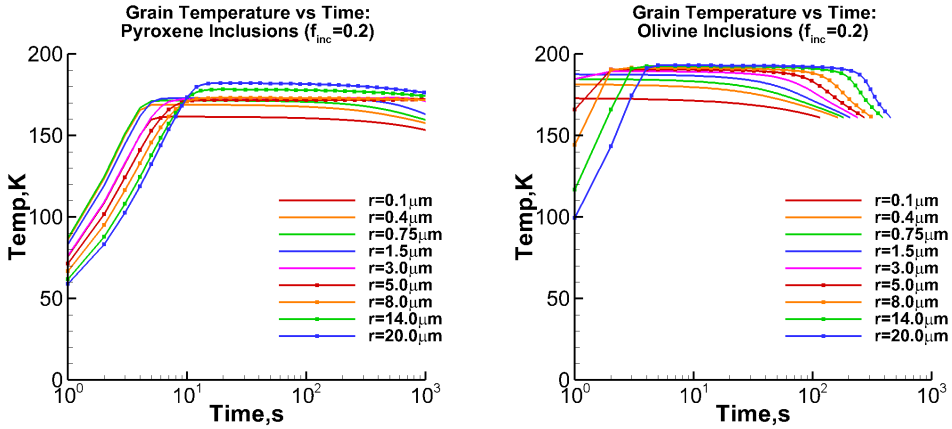

(a) Grains with pyroxene (b) Grains with olivine

Figure 5.2: Curves of grain temperature vs time for several different initial grain size. The volume fraction of regolith inclusions in the grains is f_{inc}=0.2.

The grains attain different maximum temperatures based on the in-

clusion material. Figure 5.2 shows the curves of grain temperature vs time after exposure to sunlight. The simulations are done for $f_{inc} = 0.2$ and several different initial grain sizes. The grains with inclusions quickly reach their maximum temperature, and maintain that temperature for most of their lifetime. The maximum temperature for pyroxene grains is $\sim 160 - 180$ K, while for olivine it is $\sim 170 - 190$ K. The temperature attained by grains having olivine inclusions is higher compared to grains having pyroxene inclusions which is to be expected as olivine grains absorb more energy compared to pyroxene grains and thus radiate more energy in steady state. As olivine grains radiate at a higher temperature compared to pyroxene grains, ice gets sublimated more rapidly as vapor pressure (P_{vap}) of ice varies as $e^{-\frac{1}{T}}$. Therefore, we would expect faster sublimation rate of olivine grains and thus reduced lifetimes compared to pyroxene grains.

It is seen (Fig. 5.2) that the temperature increases rapidly initially but starts decreasing after remaining constant for some period. This cooling behavior occurs at the end of the grain lifetime. Fig. 5.3 shows the grain radius vs time for several different values of initial grains radius. On carefully observing Figs. 5.1 to 5.3, we find that grains start cooling at the time when grain radius reaches values at which albedo values start tending to one ($\sim$0.1 μm for olivine grains and $\sim$0.5 μm for pyroxene grains). So as the albedo approaches one, less energy is absorbed by the grains which means that their temperature must decrease. This increase in values of albedo of the grains is the reason why the size of very small grains ($< \mathcal{O}(0.01\ \mu\text{m})$) remains constant

for a very long period. The grain lifetimes of olivine containing grains are significantly less than those of pyroxene containing grains and comparable to LCROSS timescale. The period with constant temperature for pyroxene containing grains is longer than that of olivine containing grains and exceeds or is comparable to the LCROSS timescale.

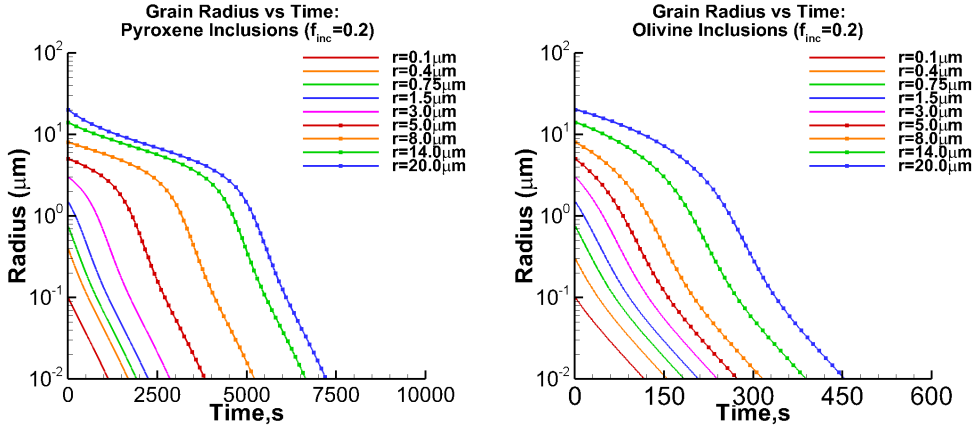

(a) Grains with pyroxene

(b) Grains with olivine

Figure 5.3: Curves of grain radius vs time for several grains that are 20% regolith by volume.

The lifetimes of the grains containing regolith are much shorter than the pure ice case (Fig. 5.4), and an increase in initial radius does not have a huge impact on the lifetime. The lifetimes of the grains with pyroxene inclusions, still exceed the LCROSS observation timescale for lower values of f_{inc}. For very high values of f_{inc} (e.g. f_{inc} =0.8), the lifetimes of the grains are comparable to and perhaps lower than the LCROSS observation timescale. Although both olivine and pyroxene are nominally dark bulk materials, they have substantially different optical properties as seen in Chapter 4. The albedo

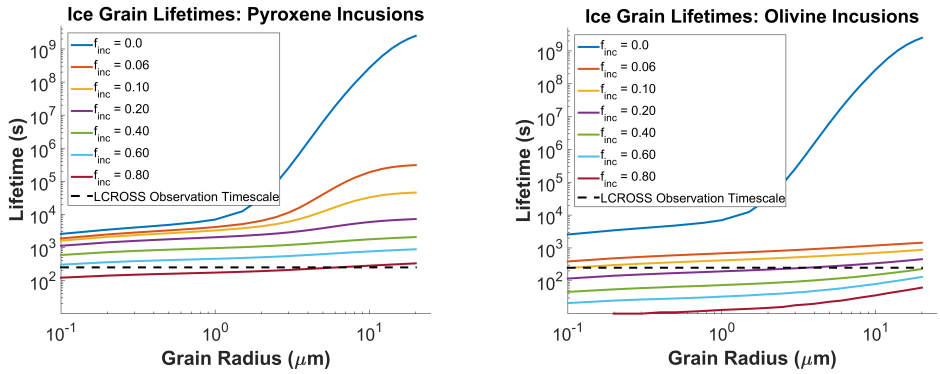

(a) Grains with pyroxene (b) Grains with olivine

Figure 5.4: Grain lifetimes for a several values of volume fraction of inclusions.

of grains containing olivine is much lower than that of grains containing pyroxene (Fig. 5.1). As a result, we observe significantly reduced lifetimes of olivine containing grains compared to pyroxene containing grains (an order of magnitude difference). Even for f_{inc}=0.2, the olivine grains sublimate at a timescale comparable to the LCROSS timescale. Thus, we expect to observe more sublimated ice vapor if there are inclusions and the inclusions are olivine.

We have discussed, in detail, the grain heating and sublimation of pure and impure ice grains using results from a standalone grain heating model. We now discuss the heating and sublimation behavior of the impure ice grains during the LCROSS event. In the standalone heating model, the ice grains are stationary and assumed to be in sunlight. However, during the LCROSS event, the ice grains are moving to and from shadow and thus behave differently. Also, as mentioned in Chapter 3, the grains in the LCROSS simulation model are made up of several simulation particles where each particle represents a certain

Table 5.1: Fraction of total ice particles that get sublimated at different times after the LCROSS impact (at t=0 s) for different values of f_{inc}.

Time after impact (s)	Total ice particles	Fraction (pyroxene)	Fraction (olivine)
f_{inc}=0.06			
10	1947000	0.000	0.020
50	1974000	0.034	0.478
100	1974000	0.072	0.690
250	1974000	0.112	0.746
f_{inc}=0.10			
10	2064000	0.000	0.043
50	2064000	0.058	0.678
100	2064000	0.120	0.832
250	2064000	0.180	0.849
f_{inc}=0.20			
10	2331000	0.001	0.103
50	2331000	0.146	0.888
100	2331000	0.274	0.927
250	2331000	0.375	0.928
f_{inc}=0.40			
10	3097000	0.013	0.218
50	3097000	0.400	0.951
100	3097000	0.609	0.955
250	3097000	0.687	0.955
f_{inc}=0.60			
10	4675000	0.041	0.319
50	4675000	0.704	0.961
100	4675000	0.842	0.962
250	4675000	0.857	0.962
f_{inc}=0.80			
10	9295000	0.114	0.400
50	9295000	0.922	0.965
100	9295000	0.937	0.966
250	9295000	0.938	0.966

number of real ice/regolith molecules. Table 5.1 presents the total number of simulated ice particles and the fraction of sublimated particles [1] for grains with inclusions for different times after the LCROSS impact. The simulations were done using 10000 grains with 1000 particles for each grain. Here, the particle refers to a simulation particle which represents a certain number of actual ice and regolith molecules. The values of volume fractions of inclusions (f_{inc}) in each grains were 6%, 10%, 20%, 40%, 60% and 80%. Even with 1.0x10^7 particles in the simulation, there is significant stochastic noise in the results. However, the results can still be used to get a qualitative understanding of the sublimation of ice grains. The total amount of pure ice (in kg) lofted due to the impact is same for all cases. As discussed in Chapter 3, only a fraction of the total grains contain ice while the rest of the grains are pure regolith, and are not tracked. Even though 1.0x10^7 particles are initialized in the simulation, only the particles which contain ice are tracked. As the volume fraction of inclusions increases, relatively less ice is present in a given grain and thus the fixed amount of lofted ice is distributed among a larger number of grains. The total number of particles in the simulation is 1.0x10^7, whereas there are fewer than 1.0x10^7 particles containing ice. The number of particles containing ice out of the 1.0x10^7 total number of particles are presented in column 2 of Table 5.1. Columns 3 and 4 give the fraction of total ice particles (column 2) that get sublimated by the given time instant (column 1) for grains

[1] For example, if grains are assumed to be 10% olivine by volume (f_{inc} =0.10), at 100 s after the impact, 83.2% of the initially lofted ice particles has been released from grains to form a water vapor cloud.

containing pyroxene and olivine respectively.

It can be seen that the ice grains sublimate quickly especially for higher values of f_{inc}. The sublimation of the grains happens rapidly in the initial period after the impact but becomes slow after $\sim$100 s; the difference between the fraction of sublimated particles at 100 s and 250 s is low compared to the difference between 10$-$50 s and between 50$-$100 s. The reason is, most of the grains in the plume reach their maximum height before 100 s and start falling back towards the lunar surface. These falling grains either get stuck on the surface or move into the shadow region of the crater (no sunlight). In both the cases, we stop tracking the grains. Only a small fraction of the total number of initial ice grains rise throughout the duration of the LCROSS observation (250 s), and sublimate. Figure 5.5 shows the distribution of grains vs grain radius for several different instances during the LCROSS event (simulation) for both pyroxene and olivine containing grains with $f_{inc} = 0.5$. The simulation is done using 10000 grains (only some of which contain ice) which are initialized using a log-normal distribution with mean radius $\sim 1\mu m$. Initially, the grains are subliming with larger grains sublimating at a higher rate i.e. the mass of ice sublimated is greater from the grains having larger radius compared to the grains having smaller radius. Therefore till 100 s, we see the peak of the distribution shifting towards left (i.e. smaller radius) and increasing in height such that the total area under the curve remains roughly constant (see blue$-$ >red$-$ >green curves). The area under the curve represents the total number of ice containing grains. After 100 s however, some of the grains which

are falling down get stuck to the ground. Therefore, we can see the height of the peak and therefore the area under the curve becoming smaller representing the loss of grains getting stuck on the ground (see purple− >orange− >pink curves). However, for some cases, especially for grains having olivine inclusions and high values of f_{inc}, the grains sublimate very quickly. As a result most of the grains get sublimated away before they fall to the lunar surface as seen in Fig. 5.5(b). Note that the size distribution of grains in both the cases is initially the same i.e. blue curves in both the figures (Figs. 5.5(a) and 5.5(b)) are the same.

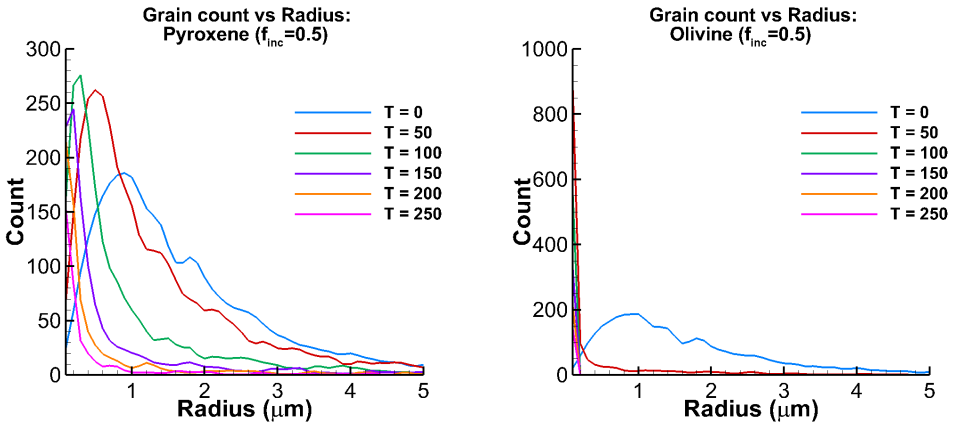

(a) Grains with pyroxene

(b) Grains with olivine

Figure 5.5: Distribution of grain radii (count) at several instances of time during the LCROSS event for grains containing pyroxene and olivine.

Fig. 5.6 shows the cloud of water vapor (column density) at 65 s for pure ice grains. Fig. 5.7 shows the column density contours of the water vapor cloud obtained from grains with regolith inclusions for $f_{inc} = 0.1$. The simulations for all these cases are done with 500000 grains with 900 particles

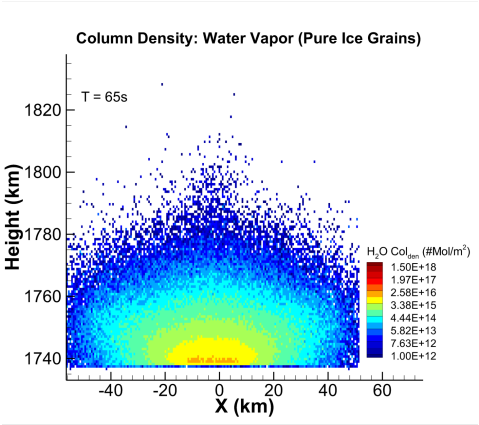

Figure 5.6: Column Density of water vapor for pure water ice.

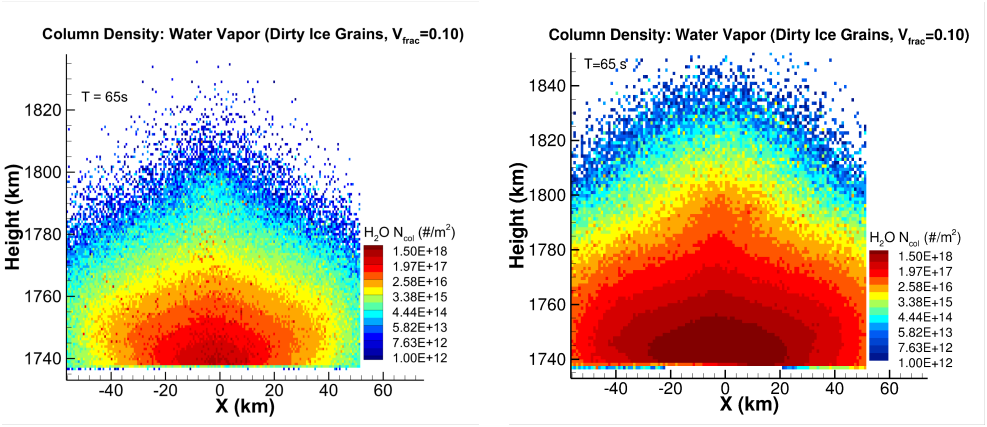

(a) Grains with pyroxene

(b) Grains with olivine

Figure 5.7: Column density of water vapor for dirty water ice. The cloud of water vapor formed due to sublimation is larger and denser due to the presence of regolith inclusions in the grains, much more so for olivine inclusions than pyroxene inclusions.

in each grain. As expected, the water vapor cloud is larger and denser when the inclusions are present in the grains and the cloud is much denser in the case of olivine constituting the inclusions. Thus, the amount of water vapor

produced not only depends on the presence of inclusions in the grains but also on the composition of the inclusions. Analyzing the presence of multiple regolith materials as inclusions in a single grain is not done in the present study. It can be done at the expense of adding more undetermined parameters characterizing the lunar regolith.

As mentioned previously, Heldmann et al. [3] employed two grain models: a pure ice/pure dirt model and an icy shell model. The model presented here is something of an intermediate between these two models. Both of the previous models were inadequate and did not correctly match the simulation results to actual observations. By fitting the simulation results to observations, we would like to obtain the nominal values of various parameters used in the simulation like f_{inc}, type of inclusions etc. to better understand the physical conditions on the surface of the Moon. This fitting has been done by ST and presented in our joint paper [].

5.1 Photodissociation of water vapor

The photodissociation model used is a basic probability check that switches a water vapor particle to an OH particle based on a random number draw to yield a dissociation rate of $8.54 \times 10^{-6}\ s^{-1}$ at 1 AU ([50]). The dissociation event is treated as a hard sphere collision between a water vapor molecule and a photon, with isotropic scattering in the center of mass frame of reference (Bird [51]). The momentum and energy conservation equations are used to calculate the velocity magnitudes of the recoiling H and OH after

dissociation, with an extra term included in the energy equation to account for the portion of excess photon energy entering translational modes. The data published by Wu and Chen [52] detailing the fraction of photon excess energy going into the internal energy modes of the products is used. From the data, the corresponding kinetic energy fraction can be determined, and thus, the recoil velocities. More details can be found in Wu and Chen [52].

Table 5.2: Mass of OH ultimately produced from t=0 to 250 s from water vapor for different values of volume fractions of inclusions in the grain (f_{inc}). The inclusions are pyroxene and olivine.

f_{inc}	M_{OH}^{vap} (g) (Olivine)	M_{OH}^{vap} (g) (Pyroxene)
6%	175	3
10%	221	9
20%	257	42
40%	274	135
60%	283	219
80%	289	271

Using the photodissociation model described above, we calculate the amount of OH produced using the LCROSS code. Table 5.2 shows the amount of OH in grams obtained from photodissociation of vapor produced through sublimation of icy grains in the LCROSS code. The values presented are the total amount of OH obtained at the end of the LCROSS event (250 s). This is not to be confused with the amount of OH in the FOV of the S-SC which is presented in Section 6.1. The simulations are run on the Stampede2 supercomputer of the Texas Advanced Computing Center (TACC) at The University of Texas at Austin, the details of which are presented in Section 6.1.

The simulations were run on 450 processors with each processor having 10000 grains with 1000 particles in each grain i.e. a total of 4.5 billion particles. The OH obtained from grains with olivine is generally much higher than that from grains with pyroxene. Even a small amount of olivine inclusions in the grains is able to produce a significantly greater amount of OH compared to pyroxene inclusions because of the higher absorption of solar energy and more rapid grain warming, as discussed previously. That is, more OH from photodissociation of sublimed vapor is obtained from olivine grains as olivine grains sublimate at a higher rate than pyroxene grains. We note that, there is a very slight increase in the amount of OH obtained from olivine grains when f_{inc} increases from 0.6 to 0.8. This slight increase occurs because of similarly high absorptivity of grains for f_{inc}= 0.6 and 0.8 (Fig. 5.1(b)). Most of the grains sublimate quickly before falling down on the lunar surface which can be seen in Table 5.1.

Chapter 6

Direct Ice Photodissociation

In the previous chapter, we discussed the photodissociation of sublimated water vapor molecules. Here, we examine the *direct* photodissociation of water *ice* molecules present in the grains due to solar irradiation. We want to know the relative significance of ice photodissociation for the LCROSS event and specifically the OH observations.

For photodissociation, photons must have sufficiently high energy to break the bond between H and OH. The energy required to break the bond, the enthalpy of dissociation (ΔH), for a water molecule is 5.12 eV. This means any photon with energy larger than ΔH, could cause the photodissociation and release an OH molecule if we neglect the binding/trapping energy of the surrounding ice. Therefore, only photons of wavelength less than 242 nm (greater than 5.12 eV energy) can initiate the process. The fraction (F_{UV}) of total solar energy contained in $0 - 242$ nm (from hereon referred to as ultraviolet (UV)) is only 0.74%. This fraction is calculated using the Planck's law for blackbody radiation with the assumption that the sun is a blackbody radiating at 5850 K [1]. Therefore the energy per unit area available for photodissociation for the

[1] Although Lyman-α radiation at 121 nm exceeds the (approximate) 5850 K blackbody

solar flux ($\dot{Q}_{sun}$) of 1373 W/m^2 at 1 AU, is very low ($\sim$ 10 W/m^2). The same energy is available for photodissociation of water vapor also. However, the photodissociation of vapor is significantly different from the photodissociation of ice. Therefore, it is necessary to find if the energy in the UV range is enough to produce significant amount of OH from ice photodissociation compared to OH from photodissociation of vapor.

As discussed in Johnson and Quickenden [34], the direct ice photodissociation is notably different from the photodissociation of water vapor. The dissociated species (H and OH) remaining within the solid ice can potentially react to reform water. This process is much more significant in the solid state than in the gas phase which is of very low density. The dissociated species get trapped between the surrounding solid molecules and may diffuse to recombine. This is known as the cage effect. The dissociated species can also react to form other species, like H_2, O_2, H_2O_2 etc. within the water ice. Also, in the solid state, the dissociated species need excess energy to overcome the binding energy of the grain in order to escape the grain. The binding energy is the cumulative attraction force exerted by the surrounding ice molecules on the dissociated species. These factors lead to a lower yield of OH in ice compared to the gas phase.

The yield of products in irradiation experiments is given by G, defined as the number of molecules produced per 100 eV of energy absorbed. For

radiation at 121 nm, the energy flux is still very low compared to integrated blackbody radiation in the UV.

a generalized definition of irradiation, the energy can be absorbed through a photon, electron, or ion bombardment. The G value is calculated from the product yield and formation cross section in experiments. Examples of such calculations can be found in Gerakines et al. [37] and Quickenden et al. [38]. Johnson and Quickenden [34] discuss the radiolysis and photolysis of water ice in outer solar system and give the G values for water ice. Delitsky and Lane ([35, 36]) also list the G values for pure H_2O and CO_2 ice and their mixture. For OH obtained from water ice, $G = 0.3$ molecules/100 eV ([34, 35, 36]) regardless of the source of irradiation. G depends weakly on surface temperature ([34]) but that dependence is neglected in this study. Also, the photodissociation yield calculations were done in laboratories using the ice sheets prepared in situ. However, photons below $\sim$ 220 nm only affect $\sim$10-30 nm top layer of ice ([36]). As the grains in our simulation have size much larger than $\sim$10-30 nm, we at first argue that we can use these yields directly for our purpose.

The amount of energy absorbed by an ice grain exposed to sunlight can be estimated by multiplying Q_{sun} and F_{UV} by the projected surface area of the grain in sunlight and the absorptance of the grains in UV. In the simulation, grains are subliming and gradually shrinking and thus we need to calculate the total area at each time step. Using the G value, the rate of production of OH molecules from each grain can be obtained. Similar calculations for the products of irradiation for the bulk ice were done by Delitsky and Lane ([35, 36]), Grundy et al. [53] and for icy grains by Grigorieva et al. [39].

To perform these calculations, we need the absorptance of each grain

at each time step. The absorptance depends on the wavelength of radiation, the radius of the ice grain and the optical properties of ice. The average absorptance over the appropriate UV range is calculated for different grain sizes using Mie theory, as described in Chapter 3. The effective refractive index is calculated using the Maxwell-Garnett mixing rule described in Chapter 5. The average absorptance is obtained by integration over the defined spectrum $(0 - 242\ nm)$ similar to Eq. (3.5).

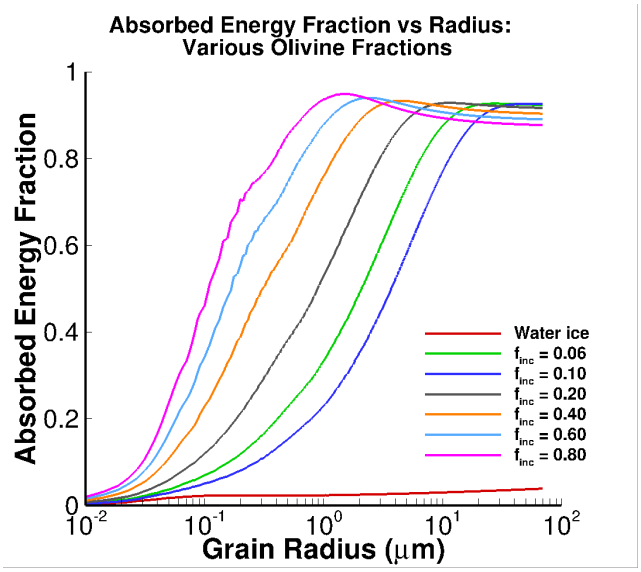

Figure 6.1: Average value of absorptance as a function of grain radius for solar radiation in $45 - 242\ nm$ for several different volume fractions of inclusions in the grain.

Using the data for olivine ([49]), the refractive index for grains with different total volume fractions of inclusions is calculated. The refractive index data ([49]) are available for $\lambda \geq$45 nm, therefore the calculations are made for the wavelength range 45-242 nm. The fraction of energy in the range 0-45

nm is anyway negligible. Figure 6.1 shows the average absorptance (fraction of energy absorbed) in the UV. The grains with inclusions absorb significantly higher energy compared to pure water ice. Even a small fraction of inclusions increases the absorption of UV energy by orders of magnitude. We select olivine to represent the inclusions in the grains for the study of direct photodissociation because of the availability of refractive index data in the ultra-violet (UV) wavelength band which is needed to study the direct photodissociation. Apart from the availability of data, there is no other reason for performing this study only for olivine.

The grains are composed of both ice and regolith molecules but only the amount of energy absorbed by ice molecules is of importance for photodissociation. The fraction of UV energy absorbed by the ice molecules might be estimated based on the mole fraction of the ice and olivine inclusions in the grains. The mole fraction can be calculated from the density and volume fraction of ice and inclusions in the ice grain. Using this approximation, the evolution of LCROSS impact plume is again simulated and the total amount of OH produced from photodissociation of water vapor and directly from water ice is calculated. These calculations are done for several different volume fractions of inclusions in the grain and presented in Table 6.1. The approximation of distributing UV energy among ice and regolith molecules based on their mole fraction in the grain is probably not a completely valid physical approximation as ice molecules by themselves absorb a very low amount of UV energy. However, the approximation can still be used to seek a conservative

estimate of the direct photodissociation process for ice grains for the LCROSS event. For the current analysis, this approximation would give us an upper bound to the amount of OH that can be obtained from the impure ice grains. The lower bound to the amount of OH produced from direct photodissociation of ice, which is negligible compared to OH produced from photodissociation of vapor, can be obtained by using the absorptivity of pure ice grains in UV (which is very low).

Table 6.1: Mass of OH produced from water vapor and directly from water ice for different values of volume fractions of inclusions of olivine in the grain (f_{inc})

f_{inc}	M_{OH}^{vap} (g)	M_{OH}^{ice} (g)	f_{inc}	M_{OH}^{vap} (g)	M_{OH}^{ice} (g)
6%	174	10	40%	274	2
10%	221	6	60%	283	1
20%	257	6	80%	289	1

Table 6.1 provides the mass of OH produced from photodissociation of water vapor arising from grain sublimation (as presented in Chapter 5) and directly from water ice for different volume fractions of inclusions in the grain. The values presented here are the total amount of OH produced by the end of the LCROSS event (250 s). The simulations were run on 450 processors on Stampede2 supercomputer (TACC) using 10000 grains with 1000 particles each per processor. The results shown are rounded to the nearest integer. These calculations are made for the nominal values of all other model parameters, as given in Heldmann et al. [3]. Because of a low number of simulation particles, the results are prone to noise but still can be used to

get a qualitative understanding of the two phenomena. The results show that the mass of OH produced from the photodissociation of water ice (M_{OH}^{ice}) is very low compared to the mass of OH produced from the photodissociation of water vapor (M_{OH}^{vap}). This is especially true for high volume fraction f_{inc} of inclusions in the grains. The amount of OH produced from vapor is directly proportional to the amount of vapor illuminated by sun. With increasing f_{inc}, the sublimation rate increases and as discussed in Chapter 5, for high values of f_{inc}, most of the illuminated ice sublimates to vapor. Thus, more vapor is formed and hence more OH is produced from vapor. On the other hand, less ice is present for the photodissociation and thus with increasing f_{inc}, less OH is produced from photodissociation of water ice. Also, although the energy absorbed by grains in the UV increases significantly with f_{inc}, the mole fraction of ice molecules in the grain decreases which limits the amount of UV energy absorbed by ice.

The OH produced from vapor photodissociation is ejected with a recoil velocity ($\sim$1 km/s) whereas OH produced from ice photodissociation is presumed to be ejected from the grain with the thermal velocity associated with the originating ice grain ($\sim$300 m/s) which is much lower than the recoil velocity. Therefore, the OH produced from ice photodissociation would stay in the FOV for a longer time than OH produced from vapor photodissociation. So, even though the net amount of OH obtained from photodissociation of ice is much less compared to that obtained from photodissociation of vapor, the OH in view by the S-SC could still be significant. Thus the direct photodis-

sociation of water ice *may* be a significant process for OH production in the LCROSS plume.

As mentioned before, the validity of approximation of distributing the UV energy absorbed by the grain among ice and olivine molecules based on their mole fractions is limited. That is, in the above approach, the photodissociation of ice was estimated based on the amount of energy absorbed by ice having regolith inclusions which is orders of magnitudes higher than what pure ice absorbs in UV (ref. Fig. 6.1). However, the effect of impurities on the absorption of UV energy by ice molecules in an impure ice grain has not been studied extensively in the literature. Therefore the need to use approximate models.

Another way of approximating the energy absorbed by ice molecules in the impure ice grains (with inclusions) would be to use the energy that would have been absorbed by the pure ice grains of the same size i.e. using $f_{inc} = 0$ line in Fig. 6.1. Through this approximation, the rate of photodissociation of ice obtained is too low to produce significant amount of OH from direct photodissociation of ice, to be viewed by S-SC. This approximation would have been valid if we were dealing with bulk ice. However, we have sub-micron ($<1\ \mu m$) sized spherical grains which should lead to a **higher** rate of photodissociation of ice as compared to bulk ice because of following reasons:

1. In such tiny grains, the binding energy would be lower than that of bulk ice. This means greater ease of escape for particles.

2. The temperature of the grains is much higher (∼200 K) than the temperature of the bulk ice samples (<100 K) used in the studies to find the rate of photodissociation of ice. This also means greater ease of escape for particles.

3. In the spherical grains, the dissociated products may be ejected from any direction whereas in bulk ice, the dissociated products can only be ejected from the top surface.

The actual increase in photodissociation rate due to these factors, however cannot be accounted for easily and this physics has not been examined in this study. We instead calculate the amount of OH produced from water ice using the photodissociation rate of water *vapor* used in Section 5.1. As discussed before, photodissociation of water vapor is substantially different from that of water ice. To account for the difference between the two processes, we multiply the photodissociation probability of vapor with a factor α, presumed to be less than one, to obtain the photodissociation probability of ice. [2]

$$\mathcal{P}_{ice} = \alpha \mathcal{P}_{vap}, \tag{6.1}$$

where $0 < \alpha < 1$. These limits on α are imposed as probability cannot be negative and the probability of photodissociation of ice should not be greater than that of vapor. α will now be another parameter in the parameter space which

[2] α for sub-micron sized icy grains could, in principle, have been obtained in a laboratory experiment but no such results could be found.

Table 6.2: Mass of OH produced from water vapor and directly from water ice for different values of volume fractions of pyroxene inclusions in the grain (f_{inc}) and probability scaling parameter α

f_{inc}	M_{OH}^{vap} (g)	M_{OH}^{ice} (g)	f_{inc}	M_{OH}^{vap} (g)	M_{OH}^{ice} (g)
α=0.01					
6%	3	3	40%	135	2
10%	9	3	60%	219	1
20%	42	3	80%	271	1
α=0.05					
6%	3	13	40%	135	5
10%	8	11	60%	218	2
20%	42	10	80%	271	1
α=0.1					
6%	3	30	40%	136	19
10%	9	29	60%	218	13
20%	42	27	80%	271	7
α=0.5					
6%	3	149	40%	135	97
10%	9	147	60%	218	63
20%	42	134	80%	271	37
α=1.0					
6%	3	296	40%	136	194
10%	9	292	60%	218	126
20%	42	267	80%	271	73

will be obtained by co-worker ST by fitting the numerical results with the S-SC observed results, similar to parameters such as f_{inc}, mean radius of grains etc. Sample calculations are also done for several different values of f_{inc} and α and presented in Tables 6.2 and 6.3. The amount of OH produced by photodissociation of vapor increases with f_{inc}, while the amount of OH produced by photodissociation of ice decreases with f_{inc}. The reason, as mentioned be-

Table 6.3: Mass of OH produced from water vapor and directly from water ice for different values of volume fractions of olivine inclusions in the grain (f_{inc}) and probability scaling parameter α

f_{inc}	M_{OH}^{vap} (g)	M_{OH}^{ice} (g)	f_{inc}	M_{OH}^{vap} (g)	M_{OH}^{ice} (g)
α=0.01					
6%	175	1	40%	274	1
10%	221	1	60%	283	1
20%	257	1	80%	289	0
α=0.05					
6%	175	8	40%	274	3
10%	221	6	60%	283	3
20%	256	4	80%	289	2
α=0.1					
6%	175	16	40%	274	7
10%	220	13	60%	282	5
20%	256	9	80%	288	4
α=0.5					
6%	175	81	40%	274	33
10%	220	62	60%	282	27
20%	256	44	80%	289	21
α=1.0					
6%	176	163	40%	273	66
10%	220	124	60%	281	53
20%	256	88	80%	289	43

fore, is the decrease in the amount of ice present for photodissociation due to increase in the sublimation rate with f_{inc}. In the case of olivine inclusions, the grains warm rapidly compared to pyroxene inclusions and the sublimation rate is very high even for small values of f_{inc}, and therefore a lower amount of OH from direct photodissociation of ice is produced. For the case of α=0.01, we obtain little OH from direct photodissociation of ice from grains having py-

roxene inclusions, but an even lower amount of OH from grains having olivine inclusions. In general, if the grains contain pyroxene inclusions, more OH from photodissociation of ice is produced compared to grains containing olivine inclusions. On the other hand, more OH from photodissociation of vapor is produced if the inclusions are olivine as opposed to pyroxene.

6.1 LCROSS OH count

As mentioned in Chapter 1, the S-SC followed nearly the same trajectory as that of the LCROSS satellite with a delay of 250 s. While moving towards the Moon's surface through the LCROSS impact plume, the S-SC observed the impact plume with the nine instruments present inside the satellite. The S-SC VSP had a FOV of a 1° cone pointing downwards towards the impact site. In the LCROSS simulation, OH molecules (produced by photodissociation) and other plume components are tracked and those present in the FOV are counted at each time step. These results can then be post-processed to obtain modeled quantities which were observed by the S-SC like OH band strength, visible spectrometer light curve etc. to compare with the actual observations. It must be noted that although many grains/ molecules are simulated, only a minor fraction of them are even within the FOV at any given time.

Figure 6.2 shows the modeled results for the total number of OH molecules in the field of view (FOV) of the shepherding satellite (S-SC) for several different values of f_{inc} and α =0.1. The simulations are carried out

on the Stampede2 supercomputer of the Texas Advanced Computing Center (TACC) at the University of Texas at Austin, Texas. We used Intel Xeon Skylake (SKX) compute nodes for our simulations. Each node has 48 Intel Xeon Platinum 8160 cores running at 2.1 GHz and each has 192 GB of memory. Each simulation is carried out on 10 nodes with tasks running on 45 processors on each node. Each process runs simultaneously on all the processors (450) with 10000 grains and 1000 particles in each grain. Simulation with more than 1×10^7 grains per core is not possible because of memory constraints. There is no communication between the processes except at the end when the results from each process are collected and averaged using Message Passing Interface (MPI). Each simulation for a particular volume fraction of olivine inclusions took 10-15 minutes of wall clock time. The differences in time for the simulations is due to adaptive substepping for the grain heating model in the code. Such large scale simulations (with $>4.5 \times 10^9$ particles) are performed to get the results which are largely free of stochastic noise.

In Fig. 6.2, we see that each curve follows a similar trend. The curve first increases rapidly and then gradually decreases. Initially, there is no OH present due to photodissociation of ice/vapor. After the impact, the grains rise above the shadow region of the crater and start sublimating and photodissociating. Therefore there is an increase in the amount of OH in the FOV of S-SC. However, at the same time, the S-SC is moving towards the lunar surface and its FOV is getting smaller with each time step. Also, OH produced from photodissociation has a very high velocity: $\sim$1000 m/s for OH from vapor and

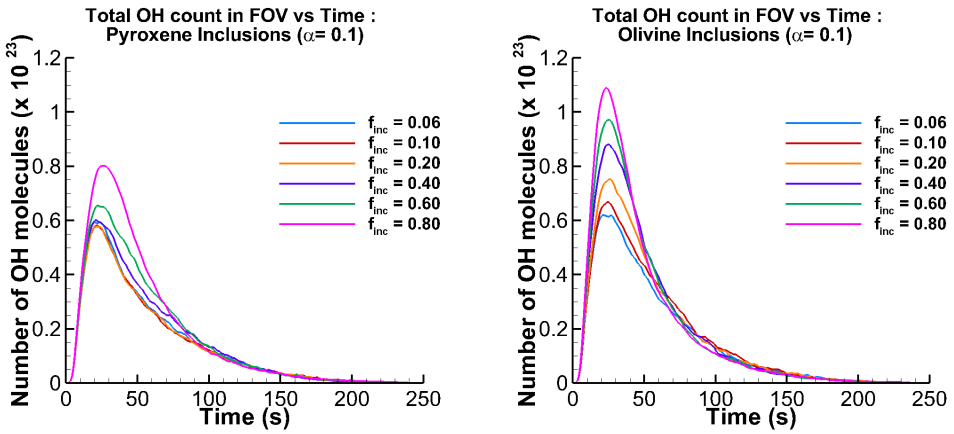

(a) Grains with pyroxene

(b) Grains with olivine

Figure 6.2: Total number of OH molecules in the FOV from photodissociation of vapor/ice molecules in the grains. The curves are for several different values of volume fraction of pyroxene and olivine inclusions.

$\sim$300 m/s for OH from ice. The OH molecules remain in FOV for a very short period of time and only a small fraction of the total OH produced is in the FOV at a given time. Therefore the amount of OH in the FOV reduces with time and goes to zero as the S-SC impacts the lunar surface. As expected, with increasing volume fraction of inclusions, more OH is produced. Grains containing olivine produce more OH compared to grains containing pyroxene.

For our joint publication [10], we acknowledge that ST worked on post processing the simulation results and fit them to the actual LCROSS observations, details of which are present in the article.

Chapter 7

Conclusions

We present an improved grain heating and sublimation model where the emission and absorption efficiency of each grain is calculated using Mie theory for electromagnetic radiation. The icy grains are assumed to have regolith inclusions and the grain properties as a function of grain size and composition are computed. The use of Mie theory to calculate optical properties of the grains is a significant improvement in the grain heating model. The first major observation is that the optical properties of the grains vary significantly with the grain size. In the previous work [3], the albedo of pure ice grains was taken as a constant value of 0.9. However, it is actually even higher than 0.95 and tends to 1.0 for the smallest grain sizes considered. Another important observation is that the sublimation rate of pure ice grains is too low to produce the significant amount of vapor in the impact plume that was observed by S-SC. Thus we consider grains with regolith inclusions which would make the grains optically darker.

By considering grains which have inclusions of pyroxene or olivine, which are the two major constituents of lunar regolith, we find a significant increase in the sublimation rate of the grains over a pure ice grain model.

However, the optical properties of olivine and pyroxene are quite different. The imaginary part of the refractive index of olivine is an order of magnitude higher than that of pyroxene in the wavelength range 0.2-4 μm, the wavelength band containing more than 99% of the solar energy. Although, both pyroxene and olivine are optically dark materials, olivine containing grains absorb and emit higher amounts of energy compared to pyroxene containing grains. We find a notable difference between the lifetime of grains having pyroxene inclusions and grains with olivine inclusions. The grains with olivine have much shorter lifetimes. The grains with regolith inclusions have higher rate of sublimation and produce a denser vapor cloud compared to pure ice grains in the LCROSS ejecta plume. A denser vapor cloud in turn means more OH is produced through vapor photodissociation.

We also study direct photodissociation of ice as a potential source of OH in the impact plume. Mie theory is used to calculate the absorption efficiency in the ultraviolet wavelength band 0-242 nm in which the photons are capable of causing photodissociation. It is found that direct ice photodissociation is also an important source of OH in the impact plume. This is especially true at high volume fraction of inclusions.

Chapter 8

Recommendations for Future Work

Several improvements can be made to the LCROSS grain model where several assumptions were made for simplification. The Mie theory model used assumes spherical grains made up of homogeneous materials as the scattering medium. However, it is highly unlikely the lofted grains are perfect spheres. Inoue et al. [32] concluded that the light scattered by an ensemble of randomly oriented dust grains can be dramatically different from that scattered by an ensemble of spheres with the same refractive index and size distribution. Mie theory has been used previously to model odd grain shapes by modeling the shapes as aggregates of spheres (Xu [54]), perhaps by introducing a suitable aggregation parameter. Implementing a similar scheme might improve the fidelity of the current model and allow for some understanding of ice grain shapes in the regolith. The requirement that grains be homogeneous is another limitation of the current grain model; the volume fraction of inclusions in a given grain is not varied. This assumption is a simplification which implies that tiny regolith particles are emitted from the subliming icy grain along with the water vapor. Further refinement of the model could allow for a non-constant volume fraction, and hence non-constant material optical properties. Of course, this would involve the introduction of additional unknown parameters. It might be

more reasonable to assume that ice condensed upon single regolith grains in the PSR. Hence, as these grains sublime away in sunlight, their ice fraction is depleted as the relative regolith fraction of the remaining core increases. The inclusions are here assumed to be made up of a single material, either pyroxene or olivine. But physically inclusions may be mixture of various components of lunar regolith in the PSR. The optical properties of different lunar materials are quite different as seen in Chapters 4 and 5. Therefore the choice of the inclusions also has a significant effect on the absorption and emission of energy which in turn affects the evolution of the grains. A study with inclusions of different materials in the grains might improve the fidelity of the modeling at the expense of introducing more unknown parameters.

The direct photodissociation of water ice is studied using the yield of OH from the experimental studies done by other researchers. The laboratory experiments utilized a thin sheet of ice to determine the yield of products obtained from photolysis/radiolysis. But we are interested in the photolysis of ice in tiny spherical grains of different sizes. A better estimate of the value of yield of OH is needed which has been determined for spherical ice grains.

References

[1] D.B. Goldstein, D.P. Summy, A. Colaprete, P.L. Varghese, and L.M. Trafton. Modeling the Vapor and Dust Dynamics Due to the Impact of the LCROSS Spacecraft on the Moon. In *AIP Conference Proceedings*, volume 1084, pages 1061–1066. AIP, 2008.

[2] D.P. Summy, D.B. Goldstein, P.L. Varghese, L.M. Trafton, and A. Colaprete. Gas and dust dynamic model of the LCROSS impacts. In *Lunar and Planetary Science Conference*, volume 41, page 2091, 2010.

[3] J.L. Heldmann, J. Lamb, D. Asturias, A. Colaprete, D.B. Goldstein, L.M. Trafton, and P.L. Varghese. Evolution of the dust and water ice plume components as observed by the LCROSS visible camera and UV–visible spectrometer. *Icarus*, 254:262–275, 2015.

[4] Solar Radiation and Climate Experiment. http://lasp.colorado.edu/home/sorce/data.

[5] J.L. Heldmann, A. Colaprete, D.B. Goldstein, D. Summy, W. Marshall, K. Ennico, M. Shirley, D. Wooden, P.L. Varghese, and L.M. Trafton. Evolution Of The Dust And Water Ice Plume Components As Observed By The LCROSS Visible Camera And UV-visible Spectrometer. In *Bulletin of the American Astronomical Society*, volume 42, page 979, 2010.

[6] P.H. Schultz, B. Hermalyn, A. Colaprete, K. Ennico, M. Shirley, and W.S. Marshall. The LCROSS cratering experiment. *science*, 330(6003): 468–472, 2010.

[7] A. Colaprete, P. Schultz, J. Heldmann, D. Wooden, M. Shirley, K. Ennico, B. Hermalyn, W. Marshall, A. Ricco, R.C. Elphic, and Others. Detection of water in the LCROSS ejecta plume. *science*, 330(6003):463–468, 2010.

[8] A. Colaprete, R.C. Elphic, J.L. Heldmann, and K. Ennico. An overview of the Lunar Crater Observation and Sensing Satellite (LCROSS). *Space Science Reviews*, 167(1-4):3–22, 2012.

[9] J.L. Heldmann, A. Colaprete, D.H. Wooden, R.F. Ackermann, D.D. Acton, P.R. Backus, V. Bailey, J.G. Ball, W.C. Barott, S.K. Blair, and Others. LCROSS (Lunar Crater Observation and Sensing Satellite) observation campaign: strategies, implementation, and lessons learned. *Space science reviews*, 167(1-4):93–140, 2012.

[10] Y. Poondla, S. Tovar, A. Agrawal, A. Mahieux, J.L. Heldmann, A. Colaprete, D.B. Goldstein, L.M. Trafton, and P.L. Varghese. Characterizing the hydroxyl observation of the LCROSS UV-Visible spectrometer: Modeling of the impact plume. (In preparation for Icarus). *The University of Texas at Austin, Texas, USA*, 2019.

[11] K. Ennico, M. Shirley, A. Colaprete, and L. Osetinsky. The Lunar Crater Observation and Sensing Satellite (LCROSS) Payload Development and Performance ináFlight. *Space science reviews*, 167(1-4):23–69, 2012.

[12] R.M. Suggs, W.J. Cooke, R.J. Suggs, W.R. Swift, and N. Hollon. The NASA lunar impact monitoring program. *Earth, Moon, and Planets*, 102 (1-4):293–298, 2008.

[13] J.R. Arnold. Ice in the lunar polar regions. *Journal of Geophysical Research: Solid Earth*, 84(B10):5659–5668, 1979.

[14] D.H. Needham and D.A. Kring. Lunar volcanism produced a transient atmosphere around the ancient Moon. *Earth and Planetary Science Letters*, 478:175–178, 2017.

[15] B.J. Butler. The migration of volatiles on the surfaces of Mercury and the Moon. *Journal of Geophysical Research: Planets*, 102(E8):19283–19291, 1997.

[16] D.H. Crider and R.R. Vondrak. Hydrogen migration to the lunar poles by solar wind bombardment of the Moon. *Advances in Space Research*, 30(8):1869–1874, 2002.

[17] B.D. Stewart, E. Pierazzo, D.B. Goldstein, P.L. Varghese, and L.M. Trafton. Simulations of a comet impact on the Moon and associated ice deposition in polar cold traps. *Icarus*, 215(1):1–16, 2011.

[18] P. Prem, N.A. Artemieva, D.B. Goldstein, P.L. Varghese, and L.M. Trafton. Transport of water in a transient impact-generated lunar atmosphere. *Icarus*, 255:148–158, 2015.

[19] A.R. Vasavada, D.A. Paige, and S.E. Wood. Near-surface temperatures on Mercury and the Moon and the stability of polar ice deposits. *Icarus*, 141(2):179–193, 1999.

[20] D.A. Paige, M. A. Siegler, J. Zhang, P.O. Hayne, E.J. Foote, K.A. Bennett, A.R. Vasavada, B.T. Greenhagen, J.T. Schofield, D.J. McCleese, and Others. Diviner lunar radiometer observations of cold traps in the Moon's south polar region. *science*, 330(6003):479–482, 2010.

[21] J. Heldmann, A. Colaprete, D. Wooden, E. Asphaug, P. Schultz, C. Plesko, L. Ong, D. Korycansky, K. Galal, and G. Briggs. Lunar Crater Observation and Sensing Satellite (LCROSS) Mission: Opportunities for Observations of the Impact Plumes from Ground-based and Space-based Telescopes. In *Bulletin of the American Astronomical Society*, volume 40, page 406, 2008.

[22] V.V. Shuvalov and I.A. Trubetskaya. Numerical simulation of the LCROSS impact experiment. *Solar System Research*, 42(1):1–7, 2008.

[23] V.V. Shuvalov. Multi-dimensional hydrodynamic code SOVA for interfacial flows: Application to the thermal layer effect. *Shock waves*, 9(6): 381–390, 1999.

[24] D.G. Korycansky, C.S. Plesko, M. Jutzi, E. Asphaug, and A. Colaprete. Predictions for the LCROSS mission. *Meteoritics & Planetary Science*, 44(4):603–620, 2009.

[25] S.S. Davis. An analytical model for a transient vapor plume on the Moon. *Icarus*, 202(2):383–392, 2009.

[26] D.M. Hurley. Modeling of the vapor release from the LCROSS impact: Parametric dependencies. *Journal of Geophysical Research: Planets*, 116 (E10), 2011.

[27] D.M. Hurley, G.R. Gladstone, S.A. Stern, K. Retherford, P.D. Feldman, W. Pryor, A.F. Egan, T.K. Greathouse, D.E. Kaufmann, A.J. Steffl, and Others. Modeling of the vapor release from the LCROSS impact: 2. Observations from LAMP. *Journal of Geophysical Research: Planets*, 117(E12), 2012.

[28] P. Artymowicz. Radiation pressure forces on particles in the Beta Pictoris system. *The Astrophysical Journal*, 335:L79—-L82, 1988.

[29] J.H. Debes, A.J. Weinberger, and G. Schneider. Complex organic materials in the circumstellar disk of HR 4796A. *The Astrophysical Journal Letters*, 673(2):L191, 2008.

[30] H. Kobayashi, S. Watanabe, H. Kimura, and T. Yamamoto. Dust ring formation due to ice sublimation of radially drifting dust particles under the Poynting–Robertson effect in debris disks. *Icarus*, 195(2):871–881, 2008.

[31] H. Kobayashi, H. Kimura, S. Watanabe, T. Yamamoto, and S. Müller.

Sublimation temperature of circumstellar dust particles and its importance for dust ring formation. *Earth, planets and space*, 63(10):6, 2011.

[32] A.K. Inoue, M. Honda, T. Nakamoto, and A. Oka. Observational Possibility of the Snow Line on the Surface of Circumstellar Disks with the Scattered Light. *Publications of the Astronomical Society of Japan*, 60 (3):557–563, 2008.

[33] E.H. Beer, M. Podolak, , and D. Prialnik. The contribution of icy grains to the activity of comets: I. Grain lifetime and distribution. *Icarus*, 180 (2):473–486, 2006.

[34] R.E. Johnson and T.I. Quickenden. Photolysis and radiolysis of water ice on outer solar system bodies. *Journal of Geophysical Research: Planets*, 102(E5):10985–10996, 1997.

[35] M.L. Delitsky and A.L. Lane. Chemical schemes for surface modification of icy satellites: A road map. *Journal of Geophysical Research: Planets*, 102(E7):16385–16390, 1997.

[36] M.L. Delitsky and A.L. Lane. Ice chemistry on the Galilean satellites. *Journal of Geophysical Research: Planets*, 103(E13):31391–31403, 1998.

[37] P.A. Gerakines, M.H. Moore, and R.L. Hudson. Carbonic acid production in H_2O:CO_2 ices. UV photolysis vs. proton bombardment. *Astronomy and Astrophysics*, 357:793–800, 2000.

[38] T.I. Quickenden, A.J. Matich, M.G. Bakker, C.G. Freeman, and D.F. Sangster. The effect of temperature on the luminescence from electron-irradiated H_2O ice. *The Journal of chemical physics*, 95(12):8843–8852, 1991.

[39] A. Grigorieva, Ph Thébault, P. Artymowicz, and A. Brandeker. Survival of icy grains in debris discs-The role of photosputtering. *Astronomy & Astrophysics*, 475(2):755–764, 2007.

[40] M.J. Cintala, L. Berthoud, and F. Hörz. Ejection-velocity distributions from impacts into coarse-grained sand. *Meteoritics & Planetary Science*, 34(4):605–623, 1999.

[41] W.J. Wiscombe and S.G. Warren. A model for the spectral albedo of snow. i: Pure snow. *Journal of the Atmospheric Sciences*, 37(12):2712–2733, 1980.

[42] E.H. Beer, M. Podolak, , and D. Prialnik. The contribution of icy grains to the activity of comets: I. Grain lifetime and distribution. *Icarus*, 180 (2):473–486, 2006.

[43] W.J. Wiscombe. Mie Scattering Calculations: Advances in Technique and Fast, Vector-Speed Computer Codes. Technical report, National Center for Atmospheric Research, Atmospheric Analysis and Prediction Division, 1988.

[44] A. Colaprete, P. Schultz, J. Heldmann, D. Wooden, M. Shirley, K. Ennico, B. Hermalyn, W. Marshall, A. Ricco, R.C. Elphic, and Others. Detection of water in the LCROSS ejecta plume. *science*, 330(6003):463–468, 2010.

[45] T. Mukai. Analysis of a dirty water-ice model for cometary dust. *Astronomy and Astrophysics*, 164:397–407, 1986.

[46] E. Hecht. *Optics*. Pearson Education, 2016.

[47] G. Heiken, D. Vaniman, and B.M. French. *Lunar sourcebook: A user's guide to the Moon*. CUP Archive, 1991.

[48] C. Jäger, H. Mutschke, B. Begemann, J. Dorschner, and Th Henning. Steps toward interstellar silicate mineralogy. 1: Laboratory results of a silicate glass of mean cosmic composition. *Astronomy and Astrophysics*, 292:641–655, 1994.

[49] B.T. Draine and H.M. Lee. Optical properties of interstellar graphite and silicate grains. *The Astrophysical Journal*, 285:89–108, 1984.

[50] M.R. Combi, W.M. Harris, and W.H. Smyth. Gas dynamics and kinetics in the cometary coma: Theory and observations. *Comets II*, 1:523–552, 2004.

[51] G.A. Bird. Molecular gas dynamics and the direct simulation monte carlo of gas flows. *Clarendon, Oxford*, 508:128, 1994.

[52] C.Y.R. Wu and F.Z. Chen. Velocity Distributions of Hydrogen Atoms and Hydroxyl Radicals Produced Throush Solar Photodissociation of Water. *Journal of Geophysical Research*, 98:7415–7435, 1993.

[53] W.M. Grundy, L.A. Young, J.R. Spencer, R.E. Johnson, E.F. Young, and M.W. Buie. Distributions of H_2O and CO_2 ices on Ariel, Umbriel, Titania, and Oberon from IRTF/SpeX observations. *Icarus*, 184(2):543–555, 2006.

[54] Y. Xu. Electromagnetic scattering by an aggregate of spheres. *Applied optics*, 34(21):4573–4588, 1995.